

<https://doi.org/10.1038/s41528-024-00309-z>

# Wireless pressure monitoring system utilizing a 3D-printed Origami pressure sensor array

Check for updates

Hadi Moeinnia<sup>1</sup>, Danielle Jaye Agron<sup>1</sup>, Carl Ganzert<sup>2</sup>, Loren Schubert<sup>2</sup> & Woo Soo Kim<sup>1</sup>

We present here a 3D-printed pressure mapping mat, equipped with customizable architecture sensors, that offers a cost-effective and adaptable solution, overcoming the size constraints and sensing accuracy issues commonly associated with existing commercial pressure mats across various fields, such as healthcare and sports applications. Leveraging a pillar-origami structure, the demonstrated sensor offers multifaceted stiffness properties, effectively filtering skin deformations and enabling capacitive pressure sensing. Notably, the sensor's detection range can be finely tuned, spanning from 70 to 2500 kPa, with a sensitivity range between 0.01 kPa<sup>-1</sup> and 0.0002 kPa<sup>-1</sup>, and an impressive response time of just 800 milliseconds. Furthermore, the inclusion of a modular sensor array enhances maintenance and allows for greater flexibility in shaping and enhancing the device's resolution. This technology finds practical applications in wireless foot pressure mapping and sports protection pads, marking a significant milestone in the advancement of flexible and custom-shaped pressure sensor technology.

Assessing pressure distribution across human limbs is of paramount significance, particularly for individuals exposed to physically demanding circumstances, such as laborers, athletes, and the elderly. Researchers employ pedobarography, a method that analyzes pressure distribution on the human foot, to identify biomechanical abnormalities during gait analysis<sup>1-3</sup>. Similarly, data derived from pressure mapping on the human foot can serve as a valuable resource for designing ergonomic insoles<sup>4</sup>. Furthermore, pressure sensors can be applied to monitor the forces exerted on human limbs during sporting activities, providing valuable insights for coaches in enhancing training methods and preventing injuries among team members<sup>5</sup>.

In response to the increasing demand for pressure data applications within wearable devices, numerous research endeavors have been undertaken to enhance the performance of pressure mapping arrays in recent years. These endeavors have primarily focused on optimizing five key performance attributes of pressure sensors, which include: 1. Pressure detection range 2. Sensitivity 3. Linearity 4. Durability and 5. Response time. This has been achieved by developing various sensor components, pressure transducing mechanisms, and manufacturing methods. Polydimethylsiloxane (PDMS), Polyimide (PI), and polyethylene terephthalate (PET) are some of the well-known flexible substrates, and silver conductive paste, gold, copper, and indium tin oxide (ITO) are some conductive

materials that are mainly used as pressure sensor electrodes<sup>6</sup>. Among the pressure transducers, piezo-resistors are known for the simple and reliable pressure sensing mechanism with high sensitivity due to the contact resistor change between sensing material and electrode<sup>7</sup>, however, resistive-based pressure sensors are largely affected by temperature changes over human activities. Piezoelectric and triboelectric pressure sensors are also proper candidates for dynamic measurement of pressure loadings, nonetheless they cannot properly work under static loading scenarios<sup>8</sup>. Finally, the capacitance mechanism can be used to measure the applied force by measuring the capacitance change due to the permeability change of dielectric and the distance change between two capacitor electrodes<sup>9</sup>.

In addition to exploring sensing mechanisms, significant attention has been devoted to the investigation of fabrication techniques. To produce conductive traces, substrates, and deposit sensing active materials, various manufacturing techniques are employed. These methods encompass a range of processes such as direct ink printing<sup>10</sup>, screen printing<sup>11</sup>, chemical or electrochemical deposition<sup>12</sup>, electrospinning<sup>13</sup> dip coating<sup>14</sup>, and lithography<sup>15</sup>. These techniques can be classified into three primary categories: force-based manufacturing, electric field-assisted manufacturing, and light-assisted manufacturing<sup>6,16</sup>. It is imperative to note that each of these fabrication processes necessitates the use of specialized equipment, controlled clean room environments, and involves multiple intricate

<sup>1</sup>Additive Manufacturing Laboratory, School of Mechatronic Systems Engineering, Simon Fraser University, Surrey V3T 0A3, Canada. <sup>2</sup>Hodgson Orthopedic Group, Coquitlam, BC V3K 6V7, Canada. ✉e-mail: [woosook@sfu.ca](mailto:woosook@sfu.ca)

manufacturing steps. Consequently, the majority of commercially available pressure mapping mats tend to be relatively high in cost. Moreover, these mats are often constrained in terms of their dimensional and array arrangement flexibility, limiting their applicability in scenarios requiring patient-specific customization. Furthermore, in instances where the pressure mapping mat sustains partial damage, such as tearing or severe impacts, the prevailing practice necessitates the complete replacement of the entire device.

Recently additive manufacturing techniques, including Filament Fused Fabrication (FFF)<sup>17</sup>, Selective Laser Annealing (SLA)<sup>18</sup>, and digital light processing (DLP)<sup>19</sup> have emerged to facilitate the customization of sensor designs and their subsequent fabrication<sup>20</sup>. The combined use of FFF and DIW techniques has gained widespread recognition to produce intricate 3D architectural sensors, renowned for their heightened sensitivity<sup>21</sup>. These sensors have found applications in a diverse range of fields, including pressure, vibration, and electromyography sensing<sup>22,23</sup>. Nonetheless, one prevailing concern that has arisen pertains to the adhesion between the sensor's structural components and electrodes in this method<sup>24</sup>.

In this study, we present a flexible pressure sensor array featuring an assembly of pillar-origami architectures. Leveraging the advantages of 3D design and 3D printing to fabricate this three-dimensional structure, the proposed architectural design offers precise control over the sensor's stiffness and its pressure measurement range. As a result, this sensor becomes highly adaptable for diverse applications in biomedicine and sports. To achieve this, we employ dual nozzle Fused Deposition Modeling (FDM) 3D printing technology. This approach allows for the simultaneous production of both the flexible sensor's structure and its conductive component in a single manufacturing step, effectively resolving the adhesion issue between layers. Furthermore, our pressure mapping array incorporates modular sensing units, granting designers the flexibility to tailor the dimensions, shape, and resolution of the pressure mapping mat to fulfill specific end-user needs. Notably, in case of sensor damage within the array, individual sensing units can be replaced, eliminating the necessity of replacing the entire device. This approach offers a cost-effective and sustainable maintenance solution, ensuring extended operational functionality.

## Results and discussion

The 3D model of the sensor was designed utilizing SolidWorks 2022 software. The pressure mapping mat comprises two essential components: 1. The array, and 2. Units. The array can be designed in different shapes and dimensions based on application and patient requirements. Moreover, each unit serves as either a sensing unit or a dummy unit (Fig. 1a). This study employs a capacitive mechanism for pressure transduction, wherein a sensing unit comprises the following components: 1. Sensor's base structure, and 2. Sensor's dielectric structure (Fig. 1b).

A dual-structure design was ingeniously incorporated into the base structure to precisely control its stiffness. This structural innovation comprises an origami tube reinforced with ribs and a central pillar (Fig. 1b), called Pillar-Origami (PO) structure. When the PO structure is pressed, initially, the pillar becomes engaged, and the origami structure of the unit remains unaffected (Fig. 1b-a). Subsequently, when the pillar buckles, both the origami and the dielectric part of the sensor become engaged, thus activating the sensor (Fig. 1b-b). Following this activation, increases in pressure cause deformation in the dielectric structure, resulting in a discernible alteration in capacitance (Fig. 1b-c). The change in electrical resistance in the dielectric structure during compression has been investigated in Supplementary Fig. 2b.

The mechanical properties of 3D structured sensors can be controlled by varying the structure's geometrical parameters, which is referred to as shape programmability in related studies<sup>24-26</sup>. In this study, a multi-stiffness structure is proposed. The stiffness of the sensor can be accurately tuned based on the application of pressure sensing mapping, determining the pressure range. Figure 2a shows the Pillar-Origami tunable geometrical parameters which are the thickness of the origami tube ( $t$ ), origami folding angle ( $\theta$ ), the diameter of the pillar ( $d$ ) the gap between the upper surface of the pillar and origami tube ( $g$ ), and the number of supporting ribs. The selection of these parameters is determined by the required pressure range and sensitivity.

The initial stiffness of the sensor is determined by the mechanical characteristics of the pillar. In this study, this determines the sensor activation threshold, however, this feature can be used for multimodal sensing applications. Upon applying the pressure, the pillar structure is compressed until it buckles, and accordingly, the sensor gets activated. The diameter of the pillar closely affects the buckling critical load and initial stiffness of the sensor. The experimental results show that the sensor's activation threshold shifts from 4 to 19 N when the diameter of the pillar varies from 1 to 2 mm, respectively, in Fig. 2b. Also, according to Euler's theory of column buckling, the stiffness of the sensor in the initial state is formulated as Eq. 1.

$$\text{Pillar stiffness : } K_p = \frac{AE}{l} = \frac{\pi d^2 E}{4l} \text{ if } F < \frac{\pi^2 EI}{l_{\text{eff}}^2} \text{ (Critical buckling load)}$$

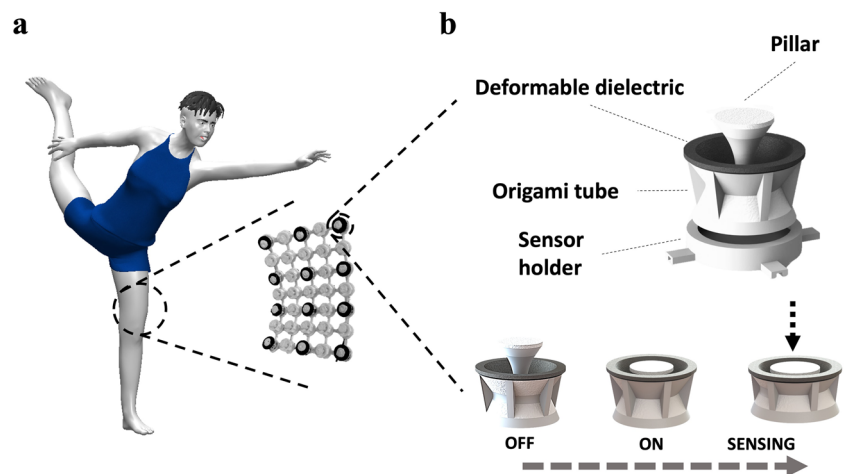
$$\text{Simplifying } \Rightarrow K_p = \frac{62.8d^2}{l} \text{ if } F < \frac{2.4 \times 10^6 d^4}{l^2}$$
(1)

Where  $K_p$  is the stiffness of pillar,  $d$  is the diameter of the pillar,  $l$  is the length of the pillar cylinder,  $A$  is the cross-section area of pillar,  $E$  is elastic modulus of TPU,  $l_{\text{eff}}$  is the effective buckling length of pillar, and  $F$  is the applied force to the pillar.

As a demonstration of an application of multi-stiffness structure for the pressure sensor, the initial stiffness of the sensor is used to remove the soft tissue deformation before the actual pressure sensing measurement.

**Fig. 1 | Pillar-Origami Pressure Mapping Mat.**

**a** Schematic of customizable Pillar-Origami pressure mapping mat for different applications of healthcare monitoring. **b** Schematic of Pillar-Origami pressure sensor unit, describing its components and characteristics in three states of ON, OFF, and Sensing.



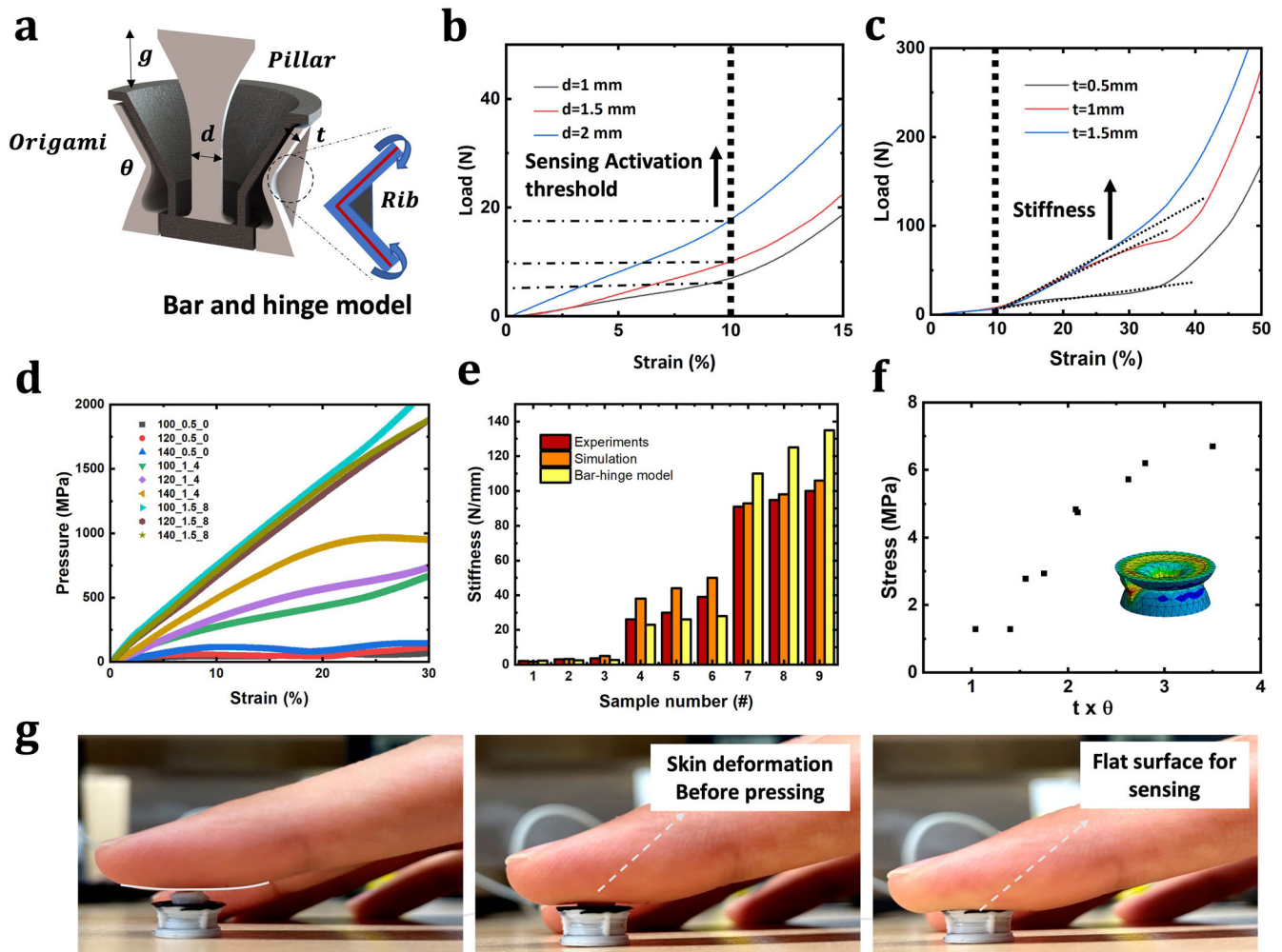


**Fig. 2 | Pillar-Origami stiffness programmability.** **a** Schematic of Pillar-Origami sensor and its geometrical parameters. **b** Effect of pillar diameter on sensing activation threshold of Pillar-Origami structure. **c** Effect of origami tube thickness on the sensor's stiffness. **d** Effect of geometrical parameters on origami tube stiffness.

**e** Comparison between the experimental results on origami tube stiffness with the predicted results of the finite element model (FEA) and bar-hinge model. **f** Von-mises stress distribution over the sensor's structure. **g** Application of multi-stiffness sensing structure for filtering the soft tissue deformation before pressure sensing.










Figure 2g shows the skin deformation caused by the pillar structure before the sensing mechanism gets activated.

The second aspect of sensor stiffness is associated with the origami tube bending behavior<sup>27</sup>, which governs the deformation of the dielectric structure during loading conditions. Accordingly, the sensitivity and pressure detection range of the sensor is accurately tuned by controlling the stiffness of the origami tube. Two geometrical parameters, including origami thickness ( $t$ ), and fold angle ( $\theta$ ) were initially used to control the stiffness of the origami tube. However, due to printing limitations, the thickness of the origami tube and its fold angle were constrained to the range of 0.6–1.5 mm and 100–140°, respectively. Moreover, during the compression of the origami tube, tube buckling was observed, which affected the behavior of the sensor (Supplementary Fig. 6). To address these issues, supporting ribs were introduced to the origami tube, providing greater stiffness tunability through control of the number of supporting ribs. Additionally, the tube buckling issue has been completely resolved. Experimental results demonstrate that the thickness of the origami tube has a significant impact on the base structure stiffness of the sensor. The stiffness of the origami tube varies from 0.9 to 4.5 N mm<sup>-1</sup> as the thickness of the origami tube changes from 0.5 mm to 1.5 mm (see Fig. 2c). To comprehensively investigate the impact of geometrical parameters on the stiffness of the sensor, we have developed a finite element model (FEM) for predicting the sensor's stiffness. The finite element model was constructed using ANSYS Workbench 2021, wherein

the sensor's structure was represented with the material properties of TPU, including an elastic modulus of 20 MPa and a Poisson's ratio of 0.2. A static analysis was conducted, applying a 20% strain compression to simulate the sensor's behavior within its pressure-sensing range. A 0.4 mm tetrahedron mesh was employed, and 3D-stress elements were selected to model stress and strain within the structure. Reaction forces and stress distributions across the sensor were measured for each simulation. Table 1 illustrates a high correlation between the finite element analysis (FEA) and experimental results. Also, the finite element model demonstrates that von-mises stress in all the samples shown in Table 1, remains below the yield strength of TPU NinjaTek Cheetah (95a), 39 MPa, ensuring that flexible pressure sensor behaves in its elastic range (Fig. 2f).

Moreover, a mathematical model was presented to predict the stiffness of the origami tube part of the sensor. Accordingly, a bar-hinge model was used to define the bending stiffness of the origami tube considering the thickness of the origami sheet thickness and origami fold angle<sup>38</sup>. The governing mathematical model is defined as shown in equation 2. Where  $K_o$  is stiffness of origami tube,  $r$  is the radius of the origami tube,  $I_n$  is rib coefficient,  $\theta$  is the fold angle,  $t$  is the thickness of the origami tube,  $\nu$  is poisson ratio,  $E$  is the elastic modulus of TPU, and  $I^*$  is the scale factor which is calculated based on the experimental data. For the set of experimental results demonstrated in Table 1, the average value for the  $I^*$  is calculated as  $10^{-6}$  (MATLAB code is attached to the

**Table 1 | Pillar-Origami pressure sensor stiffness and pressure sensing range based on geometrical parameters**

|   | <i>t</i> (mm) | <i>θ</i> (degree) | <i>d</i> (mm) | <i>g</i> (mm) | <i>Ribs</i> | Stiffness (N mm <sup>-1</sup> ) Experiments | Stiffness (N mm <sup>-1</sup> ) Simulation | Pressure (kPa) | Design  |
|---|---------------|-------------------|---------------|---------------|-------------|---|--|----------------|---|
| 1 | 0.5           | 100               | 1             | 1             | 0           | 2   | 1.75                                       | 70             |  |
| 2 | 0.5           | 120               | 1             | 1             | 0           | 3.1   | 3.2  | 130            |  |
| 3 | 0.5           | 140               | 1             | 1             | 0           | 3.7   | 5  | 130            |  |
| 4 | 1             | 100               | 1             | 1             | 4           | 26  | 38   | 800            |  |
| 5 | 1             | 120               | 1             | 1             | 4           | 30  | 44   | 900            |  |
| 6 | 1             | 140               | 1             | 1             | 4           | 39  | 50   | 1000           |  |
| 7 | 1.5           | 100               | 1             | 1             | 8           | 91  | 93   | 2500           |  |
| 8 | 1.5           | 120               | 1             | 1             | 8           | 95  | 98   | 2100           |  |
| 9 | 1.5           | 140               | 1             | 1             | 8           | 100   | 106  | 2000           |  |

**Table 2 | Supportive rib coefficients demonstrate the effect of supportive ribs on the stiffness of the origami tube**

| <i>n</i>             | 2   | 4   | 6   | 8   |
|----------------------|-----|-----|-----|-----|
| <i>l<sub>n</sub></i> | 1.4 | 1.8 | 2.2 | 2.6 |

supplementary documents).

$$\text{Hing – bar origami stiffness: } K_{\text{o}} = r l_n l^* \sin\left(\frac{\theta}{2}\right) \left(\frac{E t^3}{12(1-\nu^2)}\right) \quad (2)$$

$$\text{Simplifying } \Rightarrow K_{\text{o}} = 0.017 l_n t^3 \sin\left(\frac{\theta}{2}\right)$$

Also, rib coefficient (*l<sub>n</sub>*) is calculated by measuring the origami stiffness change while varying the number of supporting ribs on a sample with 0.5 mm origami thickness and 120° fold angle. The results of calculated *l<sub>n</sub>* are presented in Table 2.

Figure 2e shows a high correlation between the predicted stiffness in the finite element model, bar-hinge model, and experimental results within the 9 samples defined in Table 1.

The underlying sensing mechanism of the capacitive pressure sensor with a parallel plate structural design is shown in Fig. 3a. To mitigate the proximity effect of the human body on the capacitance value of the sensor, human skin can be utilized as one of the electrodes of the capacitive sensor<sup>29</sup>. Hence, one of the electrodes is directly linked to the readout board, while the other electrode for all sensors is connected to a shared reference electrode, which, in turn, is connected to the human body. This approach to measuring capacitance effectively resolves wiring concerns when scaling up the system.

The sensor’s function can be summarized in three states:

- a. **No Contact:** In this stage, human skin does not contact the dielectric structure, resulting in a low capacitance value. This value remains constant until the pillar structure buckles, causing the skin to touch the

dielectric. At this stage, all pressure values below the buckling load of the pillar are filtered out (Fig. 3a-i).

- b. **Touch:** During this stage, the human skin, which is connected to the reference electrode, contacts the dielectric. This establishes a closed capacitance measurement circuit, leading to a sudden increase in the measured capacitance of the pressure sensor (Fig. 3a-ii).
- c. **Press:** Once the dielectric structure is touched and the sensor is activated, applying higher pressure reduces the distance between the two capacitor electrodes ( $\Delta d$ ) and increases the dielectric’s permeability (as shown in Supplementary Fig. 2b). These changes result in an increased capacitance, as illustrated in Fig. 3a-iii.

To evaluate the sensor’s performance characteristics, including sensitivity, linearity, and response time, we selected a sensor with the following structure: *t* = 1 mm, *θ* = 120°, *d* = 1 mm, *g* = 1 mm, and *l<sub>n</sub>* = 4. The sensitivity of the pressure sensor is defined as the normalized capacitance change ( $\Delta C/C_0$ ) over the pressure change. Following the experimental compression tests, the sample exhibited a sensitivity of 0.005 kPa<sup>-1</sup> in the pressure range of 200–300 kPa (refer to Fig. 3c). Furthermore, the sensor demonstrated high linearity within this range (R-square = 97%). Also, Fig. 3e illustrates the sensor’s repeatability under the cyclic loading with a rate of 5 mm s<sup>-1</sup> and an 8-second on-time. The sensor’s response time was measured at 800 ms with a pulse rate of 5 mm s<sup>-1</sup>. Figure 3g showcases the sensor’s performance under various load levels, including low, medium, and high-pressure scenarios.

A finite element model was created, and an electrostatic analysis was performed using ANSYS Maxwell to evaluate the capacitive change of the pressure sensor after 20% sensor’s compression. The simulation results show a 50% increase in capacitance which is aligned with experimental results (refer to Fig. 3c). Thus, the sensitivity of the sensor can be adjusted through the manipulation of the sensor’s structural stiffness. Table 3 classifies sensor applications into three categories: soft, regular, and stiff sensors. The sensitivity range for each group is determined by the capacitance



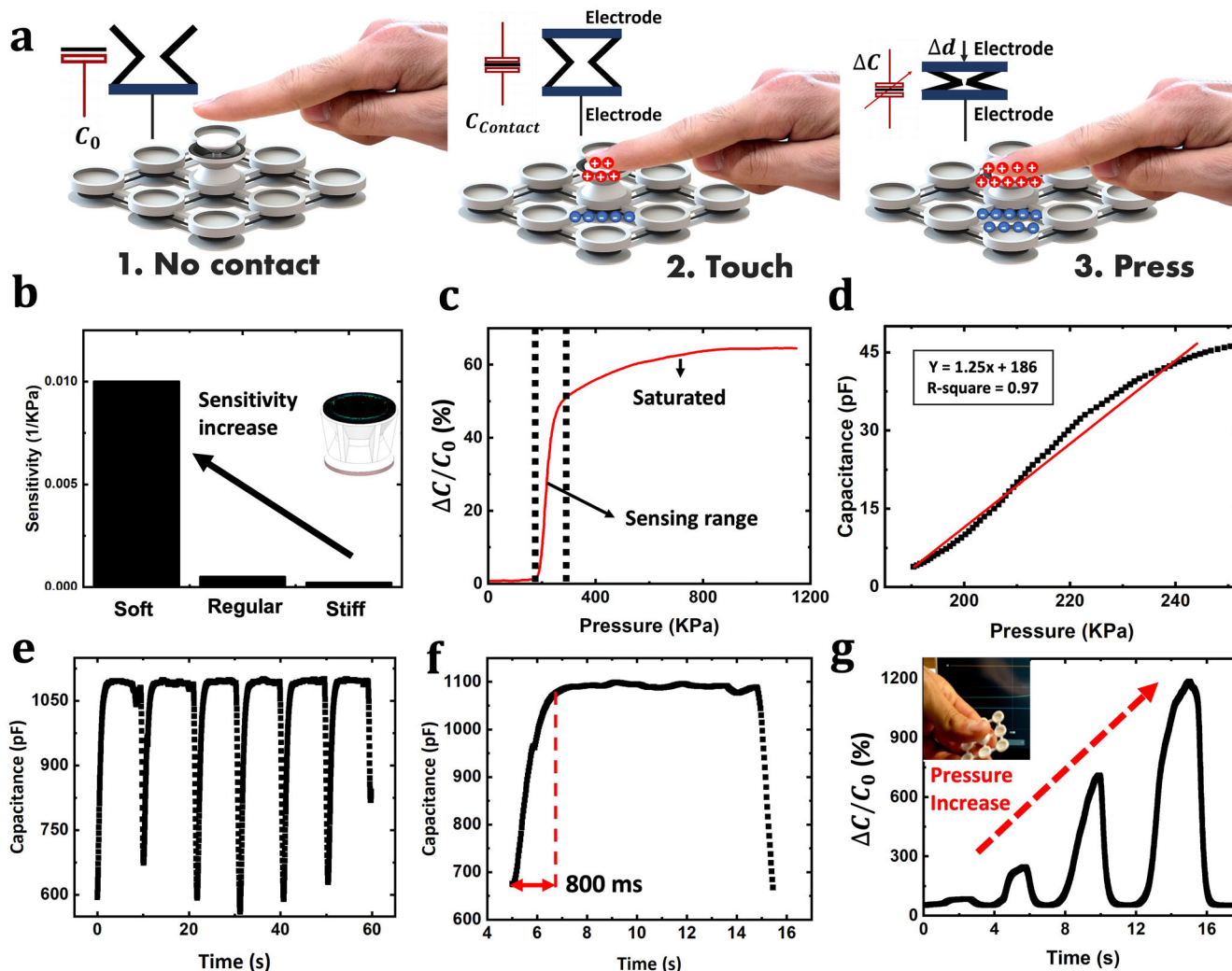


**Fig. 3 | Pillar-Origami pressure sensing performance.** **a** Schematic of the capacitive mechanism of the Pillar-Origami pressure sensor. **b** Pillar-Origami pressure sensitivity in various loading ranges. **c** Pressure sensing diagram divided into three zones: self-filtered, sensing, and saturated. **d** Linearity of the pressure sensor in the sensing zone. **e** The performance of the sensor in cyclic loading conditions. **f** Response time of the pressure sensor. **g** Demonstration of the application of different levels of loading on a pressure sensor.

change obtained in the electrostatic model using ANSYS Maxwell and the stiffness calculated in the static analysis within ANSYS Workbench. Owing to the fabrication constraints of the pressure sensor, the lowest attainable stiffness was  $2 \text{ N mm}^{-1}$ , resulting in a sensitivity of  $0.01 \text{ kPa}^{-1}$  and a loading range of 200 kPa.

In this study, we aimed to demonstrate the customizability of the proposed pressure mapping mat for various biomedical and sports applications. Two pressure mapping mat devices were designed and assembled for this purpose. The arrays and units were printed using an FDM 3D printer, and dummy/sensing units were assembled into the array after printing (refer to Fig. 4a). Each device consists of a pressure mat, a reference electrode, a data acquisition board, and a 5 V power bank to supply power to the data acquisition board. The entire device is portable, and pressure mapping results can be monitored in real-time and online (refer to Fig. 4b).

Due to the importance of measuring the pressure contour applied to the human foot during physical activities, we prepared a  $150 \times 150 \text{ mm}$  foot pressure mapping device as the initial demonstration of the proposed device. The distance between each unit was set to 15 mm, and sensing units were distributed in a  $4 \times 4$  rectangular pattern with a 30 mm distance between them, providing a sensing resolution of  $0.0011 \text{ mm}^{-2}$ . It's worth mentioning that replacing the dummy units with sensing unit, increases the sensing resolution of pressure mat. To evaluate the functionality of the pressure mapping device, we performed four distinct foot postures: i) Standing on tiptoes, ii) Normal standing, iii) Leaning to the left, and iv) Leaning to the right. The device was capable of detecting and plotting pressure concentration areas in real-time (refer to Fig. 4c).

Another innovative application of our device is measuring the impact forces exerted on protective pads during sporting activities. In this

**Table 3 | Sensitivity of the pillar-origami pressure sensors within loading ranges**

|  | Soft applications Stiffness (0–4 N/mm) | Regular applications Stiffness (4–40 N/mm) | Stiff applications Stiffness (40–100 N/mm) |
|--|--|--|--|
| Pressure range (kPa)                       | 0–200                                  | 0–1000                                     | 0–2500                                     |
| Range of Sensitivity ( $\text{kPa}^{-1}$ ) | 0.01                                   | 0.0005                                     | 0.0002                                     |

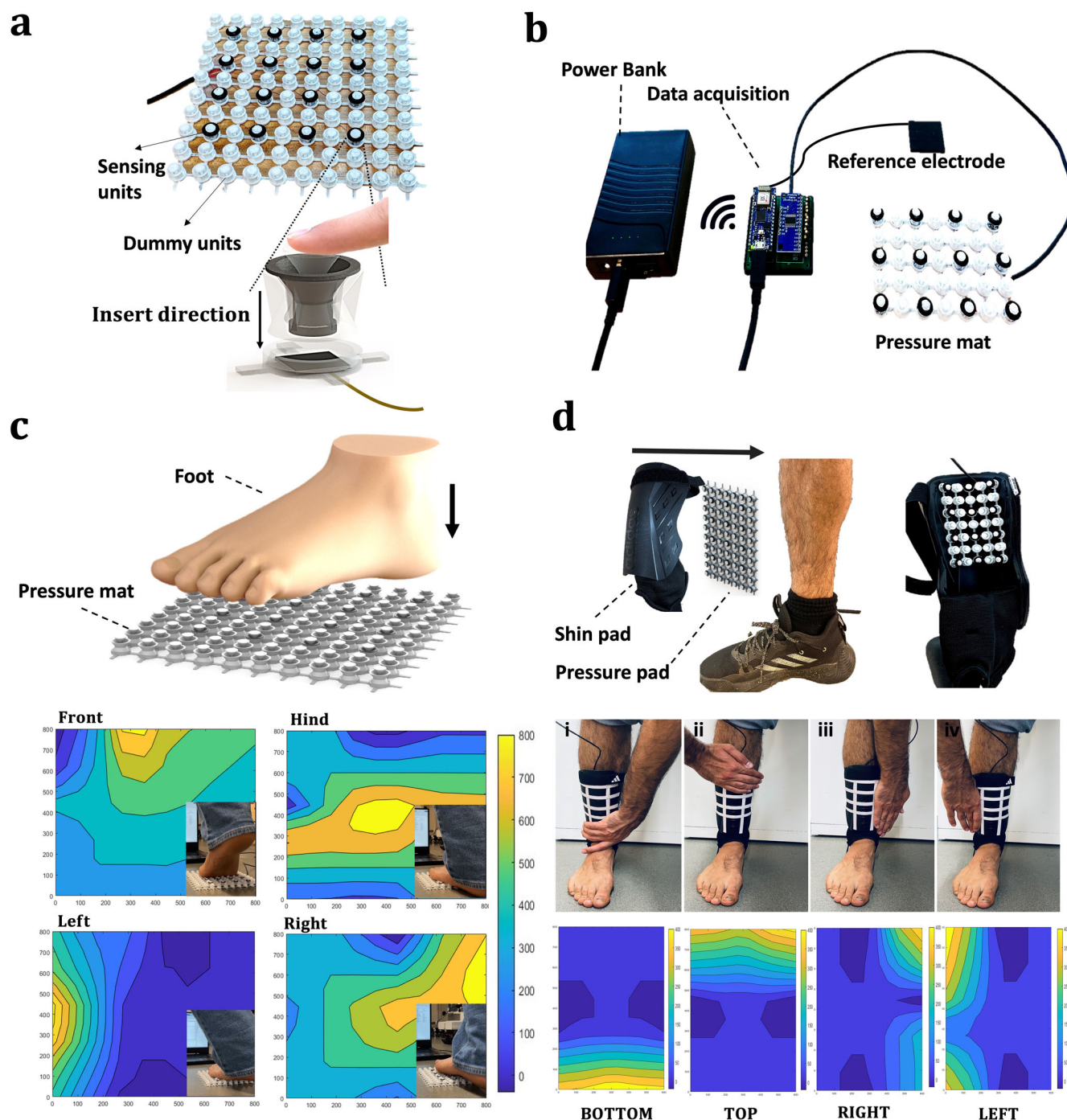


**Fig. 4 | Pillar-Origami pressure mapping mat for healthcare monitoring.** **a** Arrangement of sensing and dummy units inside the pressure mat. **b** Portable pressure mapping device. **c** Application of the designed pressure mat for foot

pressure measurement. **d** Application of the pressure mapping mat for impact detection in the shin proprioception pad.

application, we measure the pressure contour resulting from the impact on an athlete's shin. To achieve this, we printed a  $150 \times 100$  mm array with a 15 mm unit distance. Sensing units were positioned in a  $3 \times 4$  rectangular pattern with a 30 mm spacing inside the array. The pressure mat is placed inside the protective pad, which is worn on a participant's shin. We applied slight impacts to all four sides of the protective pad, including the bottom, top, left, and right. Figure 4d illustrates the device's response to these impulses.

This study addresses the dimensional constraints affecting the spatial resolution of a pressure mapping mat with a pressure array. Given our focus on applications such as prosthetics and sports devices, we aimed for a

minimum pressure resolution of 1 pressure sensor per  $500 \text{ mm}^2$ , a goal successfully attained through our research. Furthermore, to generate pressure contours with exceptional precision, we employed a natural neighbor interpolation algorithm for accurate estimation of pressure values between sensors.

In this study, the measured pressure contour demonstrates the capacitance values within each sensing unit. However, it is necessary to relate these values to the actual pressure through calibration before each measurement. The calibration process involves applying a known force to a certain number of units. Pressure is calculated by dividing the weight of the object by the contact area. The capacitance values

measured before and after applying the force are then related to the calculated pressure.

## Methods

Following the completion of Computer-Aided Design (CAD) preparations, the model is exported as an STL file and subsequently imported into the Ultimaker Cura program (Ultimaker Ltd.) to generate the G-code file for printing. For the fabrication process, we employed the Commercial 3D Printing Filament TPU NinjaTek Cheetah (95a) for creating the flexible base structural elements and the 3D Printing Filament TPU NinjaTek Eel (90 A) for printing the flexible dielectric components of the sensor. We employed a Fused Filament Fabrication (FFF) 3D printer, specifically the T-Rex 3.0 multifunctional 3D printer (refer to Supplementary Fig. 1). The printing parameters for the commercial TPU and EEL filament were meticulously configured as follows: printing speed set at 15 mm/s for TPU (10 mm/s for EEL), infill density set to 100%, printing temperature maintained at 220 °C for TPU (230 °C for EEL), and layer height set at 0.3 mm. The bed temperature was maintained at ambient room temperature throughout the printing process.

Following the preparation of each sensing unit, it is imperative to assess their proficiency in transducing pressure into an electrical signal. This evaluation process necessitated the utilization of a compression test station in conjunction with a data acquisition board. Mechanical compression loading was executed using the EZ-LX tensile test machine, while capacitance measurements were conducted employing an Arduino Uno microcontroller. The procedure for measuring capacitance entailed the application of a 5 V voltage pulse with a duration of 5 nanoseconds to one electrode of the sensor. Subsequently, the voltage across the other electrode was measured after a delay of 30 nanoseconds, thereby establishing the capacitance value. This approach for capacitance measurement is readily accessible through the Arduino library as Capacitor and is compatible with a range of microcontroller architectures, including AVR, SAM, and PIC 32. Furthermore, the analog signal processing involved a three-step low-pass filtering strategy to effectively eliminate extraneous noise signals stemming from unforeseen mechanical, electrical, and electromagnetic interferences<sup>30,31</sup>. The cutoff frequencies for the first, second, and third low-pass filters were configured at 20 Hz, 10 Hz, and 5 Hz, respectively. Arduino codes for capacitance measurement and signal processing are provided in supplementary information note B.

To achieve comprehensive pressure contour measurements across the human limb, the deployment of multiple sensing units within a sensing array is imperative. Determining the requisite number of sensing units, along with the shape and dimensions of the pressure mapping array, should be contingent upon the requirements of the patient and the application. To facilitate collecting of pressure sensing data from all these sensing units, a high-speed 16-channel analog multiplexer, specifically the CMOS CD74HC4067, was employed. A custom-designed data acquisition board, which incorporates the multiplexer along with an Arduino Nano IoT, was meticulously designed and prepared. The layout of the data acquisition circuit is elaborated upon in the Supplementary Fig. 4.

To transmit data from each sensor, 34 AWG Enameled copper wires were meticulously employed. The terminal ends of these enameled wires were meticulously stripped of their enamel coatings using specialized sanding tools to ensure precise electrical connectivity at sensing electrodes (refer to Supplementary Fig. 5). After setting up the pressure sensing array, the Arduino Nano IoT is used to serve as a dedicated server, dispatching the acquired pressure data to all connecting clients. The code responsible for this process of measuring and transferring sensor data is appended to the supplementary documents.

Within this study, a MATLAB script is used to receive wireless data from the data acquisition board and contour plot the sensing data. To initiate the pressure mapping process, it is imperative to first define the locations of the sensor units within the pressure mapping mat. This is achieved by creating a matrix that corresponds to the dimensions of the pressure mapping mat. The values within each cell of this sensor matrix

dictate the precise location of each sensing unit. The customization of sensor placement within the pressure mapping mat is flexibly accommodated to align with the specific physical requirements. Upon the exact definition of the sensor locations and their associated pressure values read from the data acquisition circuit, the scattered Interpolant function within MATLAB, configured with a natural interpolation setting, is invoked. This setting ensures that the pressure mapping results exhibit first-order continuity throughout the defined pressure mapping mat. MATLAB codes are thoughtfully provided within the supplementary documents.

The research procedures for measuring pressure data on participant's limb have received approval from the Research Ethics Committee at Simon Fraser University in Canada under the application number 3001671. A 27-year-old male volunteer, who had no previous medical history of mental health conditions, physical disabilities, orthopedic disorders, and skin issues was recruited to participate in this study's experiments. The individual provided signed consent, including permission for photography and video recording during the test, and consent for the recorded data to be used for publication. We strictly adhere to Canadian legal standards, ensuring the utmost confidentiality of all participants.

## Data availability

The datasets, including experimental data and simulation models, used in the current study, are publicly available from the online repository at <https://vault.sfu.ca/index.php/s/BTXPbQP7CuOo15>.

## Code availability

All codes used for the measurement and data analysis are provided in the supplementary documentation.

Received: 5 November 2023; Accepted: 22 March 2024;

Published online: 03 April 2024

## References

1. Lorkowski, J., Gawronska, K. & Pokorski, M. Pedobarography: A Review on Methods and Practical Use in Foot Disorders. *Appl. Sci.* **11**, 11020 (2021).
2. Jeon, E. & Cho, H. A Novel Method for Gait Analysis on Center of Pressure Excursion Based on a Pressure-Sensitive Mat. *Int. J. Environ. Res. Public Health* **17**, 7845 (2020).
3. Duan, Y., He, S., Wu, J., Su, B. & Wang, Y. Recent Progress in Flexible Pressure Sensor Arrays. *J. Nanomater.* **12**, 2495 (2022).
4. Jafarzadeh, E., Soheilifard, R. & Ehsani-Seresht, A. Design optimization procedure for an orthopedic insole having a continuously variable stiffness/shape to reduce the plantar pressure in the foot of a diabetic patient. *Med. Eng. Phys.* **98**, 44–49 (2021).
5. Raza, T. et al. Wearable and Flexible Multifunctional Sensor Based on Laser-Induced Graphene for the Sports Monitoring System. *ACS Appl. Mater. Interfaces* **14**, 54170–54181 (2022).
6. Huang, Y., Fan, X., Chen, S.-C. & Zhao, N. Emerging Technologies of Flexible Pressure Sensors: Materials, Modeling, Devices, and Manufacturing. *Adv. Funct. Mater.* **29**, 1808509 (2019).
7. Tan, Y. et al. A Soft Wearable and Fully-Textile Piezoresistive Sensor for Plantar Pressure Capturing. *Micromachines (Basel)* **12**, 110 (2021).
8. Zhi, C., Shi, S., Si, Y., Fei, B., Huang, H. & Hu, J. Recent Progress of Wearable Piezoelectric Pressure Sensors Based on Nanofibers, Yarns, and Their Fabrics via Electrospinning. *Adv. Mater. Technol.* **8**, 2201161 (2023).
9. Shi, Y. et al. Flexible capacitive pressure sensor based on microstructured composite dielectric layer for broad linear range pressure sensing applications. *Micromachines (Basel)* **13**, 223 (2022).
10. Rocha, V. G., Saiz, E., Tirichenko, I. S. & García-Tuñón, E. Direct ink writing advances in multi-material structures for a sustainable future. *J. Mater. Chem. A Mater.* **8**, 15646–15657 (2020).
11. Zhou, Z. et al. Supersensitive all-fabric pressure sensors using printed textile electrode arrays for human motion monitoring and



- human-machine interaction. *J. Mater. Chem. C. Mater.* **6**, 13120–13127 (2018).
12. Liu, M. et al. CNT/STF/Kevlar-based wearable electronic textile with excellent anti-impact and sensing performance. *Compos Part A Appl. Sci. Manuf.* **126**, 105612 (2019).
  13. Wang, Z., Si, Y., Zhao, C., Yu, D., Wang, W. & Sun, G. Flexible and Washable Poly (Ionic Liquid) Nanofibrous Membrane with Moisture Proof Pressure Sensing for Real-Life Wearable Electronics. *ACS Appl. Mater. Interfaces* **11**, 27200–27209 (2019).
  14. Lian, Y., Yu, H., Wang, M., Yang, X. & Zhang, H. Ultrasensitive Wearable Pressure Sensors Based on Silver Nanowire-Coated Fabrics. *Nanoscale Res. Lett.* **15**, 70 (2020).
  15. Maharshi, V., Sharma, S., Prajesh, R., Das, S., Agarwal, A. & Mitra, B. A Novel Sensor for Fruit Ripeness Estimation Using Lithography Free Approach. *IEEE Sens J.* **22**, 22192–22199 (2022).
  16. Zhang, J., Zhang, Y., Li, Y. & Wang, P. Textile-Based Flexible Pressure Sensors: A Review. *J. Polym. Res.* **62**, 65–94 (2022).
  17. Barši Palmić, T., Slavič, J. & Boltežar, M. Process Parameters for FFF 3D-Printed Conductors for Applications in Sensors. *J. Sens.* **20**, 4542 (2020).
  18. Seo, M., Hwang, S., Hwang, T. & Yeo, J. Fabrication of Soft Sensor Using Laser Processing Techniques: For the Alternative 3D Printing Process. *J. Mater.* **12**, 2955 (2019).
  19. Xiao, T., Chen, Y., Li, Q., Gao, Y., Pan, L. & Xuan, F. All Digital Light Processing-3D Printing of Flexible Sensor. *Adv. Mater. Technol.* **8**, 2201376 (2023).
  20. Cardoso, R. M. et al. Additive-manufactured (3D-printed) electrochemical sensors: A critical review. *Anal. Chim. Acta* **1118**, 73–91 (2020).
  21. Bao, C., Moeinnia, H., Kim, T.-H., Lee, W. & Kim, W. S. 3D Structural Electronics Via Multi-Directional Robot 3D Printing. *Adv. Mater. Technol.* **8**, 2201349 (2023).
  22. Su, H., Moeinnia, H. & Kim, W. Printed Electromyography Sensing System. *Adv. Sens Res.* **2**, 2300003 (2023).
  23. Moeinnia, H., Su, H. & Kim, W. S. Novel Grasping Mechanisms of 3D-Printed Prosthetic Hands. *Adv. Intell. Syst.* **4**, 2200189 (2022).
  24. Su, H., Kim, T.-H., Moeinnia, H. & Kim, W. A 3D-Printed Portable Wristband for Quantitative EMG Analysis. *IEEE Sens J.* **23**, 7895–7902 (2023).
  25. Kim, T.-H., Bao, C., Chen, Z. & Kim, W. S. 3D printed leech-inspired origami dry electrodes for electrophysiology sensing robots. *npj Flex. Electron.* **6**, 5 (2022).
  26. Kim, T., Vanloo, J. & Kim, W. S. 3D Origami Sensing Robots for Cooperative Healthcare Monitoring. *Adv. Mater. Technol.* **6**, 3 (2021).
  27. Zhao, S., Zhang, Y., Wu, H., Zhang, Y., Yang, J. & Kitipornchai, S. Tunable nonlinear bending behaviors of functionally graded graphene origami enabled auxetic metamaterial beams. *Compos Struct.* **301**, 116222 (2022).
  28. Woodruff, S. R. & Filipov, E. T. A bar and hinge model formulation for structural analysis of curved-crease origami. *Int J. Solids Struct.* **204–205**, 114–127 (2020).
  29. Zhu, Z., Li, R. & Pan, T. Imperceptible Epidermal-Iontronic Interface for Wearable Sensing. *Adv. Mater.* **30**, 1705122 (2018).
  30. Shu, Y., Li, C., Wang, Z., Mi, W., Li, Y. & Ren, T.-L. A Pressure Sensing System for Heart Rate Monitoring with Polymer-Based Pressure Sensors and An Anti-Interference Post Processing Circuit. *J. Sens.* **15**, 3224–3235 (2015).
  31. Kim, T.-H., Moeinnia, H. & Kim, W. S. 3D printed vorticella-kirigami inspired sensors for structural health monitoring in Internet-of-Things. *Mater. Des.* **234**, 112332 (2023).

## Acknowledgements

The authors acknowledge the financial support from the Natural Sciences and Engineering Research Council of Canada (NSERC) and Hodgson Orthopedic Group.

## Author contributions

W.S.K. conceived the concept of the origami-based pressure mapping mat for biomedical applications and supervised the project. H.M. designed the architected pressure mapping mat and conducted the experiments, with assistance from D.J.A. in analyzing the measurements. C.G. and L.S. contributed to discussions regarding the performance and analysis of the architected pressure sensor mat. All authors participated in writing and revising the manuscript.

## Competing interests

The authors declare no competing interests.

## Additional information

**Supplementary information** The online version contains supplementary material available at <https://doi.org/10.1038/s41528-024-00309-z>.

**Correspondence** and requests for materials should be addressed to Woo Soo Kim.

**Reprints and permissions information** is available at <http://www.nature.com/reprints>

**Publisher's note** Springer Nature remains neutral with regard to jurisdictional claims in published maps and institutional affiliations.

**Open Access** This article is licensed under a Creative Commons Attribution 4.0 International License, which permits use, sharing, adaptation, distribution and reproduction in any medium or format, as long as you give appropriate credit to the original author(s) and the source, provide a link to the Creative Commons licence, and indicate if changes were made. The images or other third party material in this article are included in the article's Creative Commons licence, unless indicated otherwise in a credit line to the material. If material is not included in the article's Creative Commons licence and your intended use is not permitted by statutory regulation or exceeds the permitted use, you will need to obtain permission directly from the copyright holder. To view a copy of this licence, visit <http://creativecommons.org/licenses/by/4.0/>.

© The Author(s) 2024